Supplementary information for "Facet-dependent growth and dissolution of hematite resulting from autocatalytic interactions with Fe(II) and oxalic acid"

Sandra D. Taylor,[a] * John B. Cliff,[b] [+] Thomas Wietsma,[b] Kevin M. Rosso[a] *

[a] Physical and Computational Sciences Directorate, Physical Sciences Division, Pacific Northwest National Laboratory, Richland, WA 99352, USA.

[b] Earth and Biological Sciences Directorate, Pacific Northwest National Laboratory, Richland, WA 99352, USA

[+] New address: National Security Directorate, Oak Ridge National Laboratory, Oak Ridge, TN 37830, USA

*Corresponding authors: sandra.taylor@pnnl.gov, kevin.rosso@pnnl.gov

Section 1: General batch experimental conditions

Two different batch experiments were conducted, described in the main text. In general, experiments were conducted in an anoxic glovebox (93% N_2 / 7% H_2 atmosphere) and all solutions were mixed using anoxic, degassed water. The water was prepared by boiling ultrapure Milli-Q water in Pyrex Corning glass bottles on a hot plate for ~30 minutes under vacuum, and then sparging it with purified N_2 in the glovebox. Stock solutions of 0.08 M ^{57}Fe(II) (96% ^{57}Fe, Cambridge isotopes) in 0.3 M HCl (trace metal basis) and 0.1M KCl were prepared beforehand and stored in the glovebox. A 0.08 M $FeCl_2$ solution was also premade for the control ^{NA}Fe-oxalate-hematite reactions. A 0.1 M stock oxalic acid (99.9% purity) solution was prepared the day of the experiment. The stock solutions were diluted in amber polypropylene centrifuge tubes to the appropriate concentrations for the respective solutions, reserving aliquots for aqueous analyses. We note the dilution of oxalic acid in water to 10 mM naturally led to the pH of interest (i.e., ~pH 2.3 - 2.4). Solutions without oxalic acid (e.g., 10 mM KCl) were diluted in a stock pH 2.3 solution, titrated with 1M HCl. Care was taken to avoid exposing the solutions with Fe(II)-oxalic acid to light to prevent potential photoreduction reactions, by working away from light and using amber tubes.

The supernatant was removed via centrifugation and filtered through a 0.22 μm membrane to remove particulates, again avoiding exposure to light, and reserved for aqueous analysis. Weakly bound Fe(II) on the hematite was removed by rinsing the particles with water and exposing them to 0.4 M HCl for 10 minutes. This allowed us to feature more specifically the strongly interacting Fe(II) fraction, such as that attributable to the process of oxidative adsorption consistent with surface recrystallization. Following the acid extraction step, the particles were rinsed two more times with the anoxic Milli-Q water and dried overnight.

Section 2: Multimodal characterization

2.1 UV-Vis and ICP-MS analysis

Iron concentrations in solution and their isotopic composition were determined using ultraviolet-visible spectroscopy (UV-Vis) and inductively coupled mass spectrometry (ICP-MS), respectively. $Fe(II)_{aq}$ before and after reaction was measured using the ferrozine method.[1] Aliquots of the solution before and after the reaction were diluted to <0.025 mM and equilibrated to pH 7.5 in a HEPES buffered solution with 1 mM ferrozine. Measurements were acquired on a UV-vis spectrophotometer using a wavelength of 562 nm. To account for soluble Fe(III) present ($Fe(III)_{aq}$), hydroxylamine hydrochloride was added to the aliquot to reduce iron in solution to Fe(II) and equilibrated for one day prior to adding ferrozine and measurements with UV-vis. Total iron concentrations (Fe_{tot}) were obtained, and $Fe(III)_{aq}$ was in turn inferred from the difference between Fe_{tot} and $Fe(II)_{aq}$. Aqueous iron concentrations in solution were quantified using a simple linear standard calibration curve, based on five different concentrations. The analytical precision for the aqueous iron concentrations was better than 4% relative standard deviation (RSD) based on duplicate measurements of the standards.

The aliquots were also analyzed with ICP-MS to measure the iron isotopic composition. In particular, the isotopic fraction of ^{56}Fe and ^{57}Fe was analyzed to follow extent of iron atom exchange resulting from mixing during contact between the ^{57}Fe-spiked solution vs. ^{56}Fe-dominant hematite. These measurements were carried out using an Agilent Technologies 7500 ICP-MS. Using the Fe_{tot} measurements from UV-Vis, the aliquots were diluted to ~0.5 μM (30 ppb) in 0.1M HCl-trace metal basis. Measurements were performed in pulse-counting mode using a collision cell with pure He gas, to remove potential interferences from argide polyatomic species (e.g., $^{56}[ArO]^+$, $^{54}[ArN]^+$). ^{54}Fe, ^{56}Fe, ^{57}Fe, and ^{58}Fe were measured. ^{60}Ni was also measured to correct for interferences between ^{58}Ni on ^{58}Fe, which was generally negligible. ^{72}Ge was also used as an internal standard. A 0.1M HCl blank was used to correct for background. f_{57Fe} was quantified based on a simple linear standard calibration curve across seven different ^{57}Fe concentrations. The analytical precision for f_{57Fe} measurements was better than 7% RSD based on duplicate measurements of the standards.

2.2 AFM analysis

For the atomic force microscopy (AFM)-centric experiments, the goal was to monitor dissolution/growth processes on hematite following reaction, by following microtopographic changes in the same single crystallites before and after reaction. To enable these measurements, ~0.5 mg of the hematite microplatelets was dispersed onto 10mm vitreous carbon planchets (Ted Pella) using isopropanol. The substrate was dried in a vacuum desiccator and loose particles were blown off the substrate. The specimens were then plasma cleaned with O_2 for ~30 minutes to remove C residue. AFM measurements (Veeco Icon) over several particles for each planchet were collected before reaction in contact mode. Standard silicon nitride tips were used; the applied tip force was minimized to <2nN to reduce chances of dislodging a particle. Image areas were generally 10 – 30 μm to capture the entire particle, with lines per samples of 256-512 and scan rates at 0.25 – 0.5 Hz. Particle locations were identified relative to fiducial markers on the substrate (e.g., roman numerals scratched into the substrate).

Batch reaction experiments were conducted similar to the bulk batch experiments, using the Parr acid digestion vessel setup. To minimize particles from being dislodged from the planchet during mixing in the oven, the planchet was adhered to the bottom of the 23mL Teflon cup using double-sided tape. These additional variables introduced (e.g., the planchet, double-sided tape, etc.,) were not found to affect measurements as the particle microtopography for the standard KCl-hematite* reaction could be reproduced within error. The 12.5 mL of the respective solution was added to Teflon cup, which was then sealed and reacted in the rotary oven at 75°C for 24h, as done for the loose powder experiments. Following reaction, the Parr bombs were quickly cooled in the ice bath and transferred into the glovebox.

The supernatant was removed and reserved for aqueous analysis. The specimens were washed in the Teflon cups with 5 mL pH 2.3 solution three times to remove residual reactants from particle surfaces. Minimal cleaning was done to again prevent particles from being dislodged from the planchet to enable post-reaction AFM imaging of the identical particles that were characterized pre-reaction. The specimens

were dried in the glovebox and the particles of interest were imaged with AFM after reaction, following the same protocol used for the before-reaction imaging.

To distinguish net dissolution vs. growth along the [001] direction of the tabular platelets, thicknesses of identical particles were measured relative to the underlying substrate before and after reaction. The substrates were high-purity vitreous carbon planchets (10 mm diameter), which provided sufficiently smooth reference surfaces (e.g., ~10 – 20 nm RMS roughness). Topographic AFM images enabled quantitation of changes in the surface microtopography; Z-sensor images were chosen over height images as it provides more accurate heights for features > 1 μm, as needed for the ~1 – 3 μm thick platelets used here. The images were processed in Gwyddion, a 2D analysis tool (v. 2.54).[2] Corrections were applied (e.g., mean plan subtraction, polynomial background removal) until an effectively flat planchet reference surface was obtained, designated as zero height. Deflection images were collected along with the topographs to more easily detect and qualitatively characterize fine-scale morphologic changes (Figure S1). The heights of the basal surface were measured to determine whether growth or dissolution was prevalent. The basal surface height across a single particle often varies by several hundred nanometers due to the particle microtopography (e.g., growth spirals and terraces), as shown by 2D height profiles. Thus, 2D profiles in select areas were used to highlight changes in particle height across two distinct features (e.g., corner to corner).

To quantify the change in the basal surface heights across all the particles, mean height measurements were used and compared between the before and after images. This was obtained by using the Row/Column statistics module in Gwyddion. The basal surfaces for the before and after reaction z-sensor images were isolated as a masked region. A bounding box was also drawn and positioned in the specific locations minimizing inclusion of heights from edge facets. The module could then determine the mean height of the basal surface and the standard deviation (SD) which was typically at the nanometer scale.

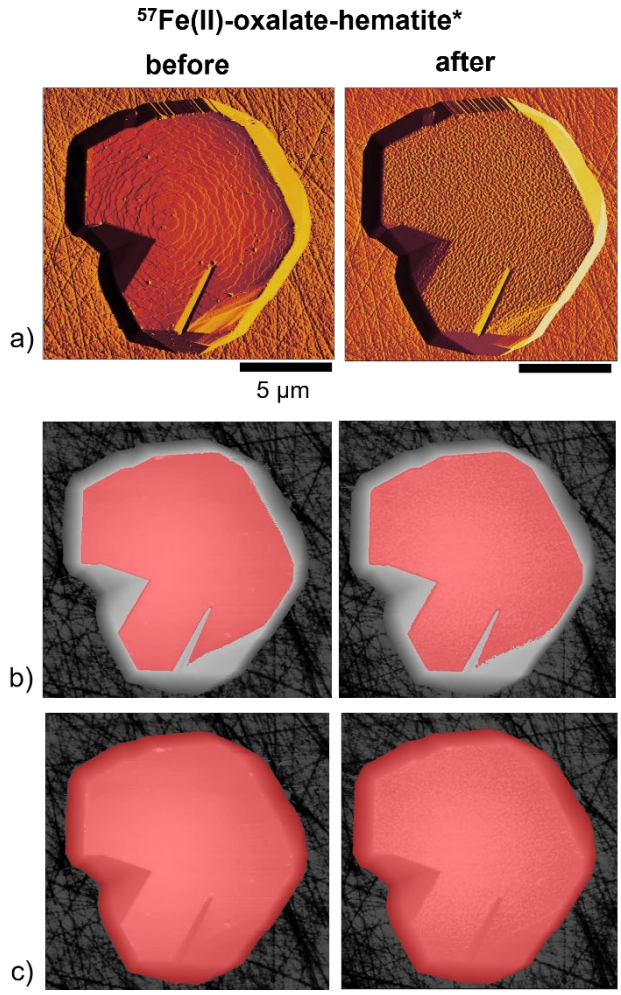

Figure S 1: (a) Deflection imaging on a particle from the ^{57}Fe-oxalate-hematite reaction, and corresponding z-sensor images showing the masks applied for (b) average basal and (c) average diameter or length analyses.*

The change in the basal surface height (Δz) was calculated from the average basal heights before and after reaction ($z_{BR,avg}$ and $z_{AR,avg}$, respectively) (Eqn. 1) along with the corresponding SD (Eqn. 2).

$$\Delta z = z_{AR,avg} - z_{BR,avg} \quad (1)$$

$$SD = \sqrt{SD_{BR,avg}{}^2 + SD_{AR,avg}{}^2} \quad (2)$$

Similarly, changes in particle diameters ($\Delta d_{particle}$) were also measured by isolating and masking the entire particle in z-sensor images obtained before and after reaction. The average length was obtained from the Row/Column statistics module. For these calculations, particle SD is large relative to $\Delta d_{particle}$, as the particle diameter is non-uniform and varies at the micrometer scale.

2.3 NanoSIMS analysis

Nanoscale secondary ion mass spectrometry (NanoSIMS) was used to characterize the hematite platelets in a manner similar to that described in Taylor*, et al.* [3]. This approach was applied here to examine Fe isotopic compositions of the hematite particle surfaces after reaction with ^{57}Fe(II), seeking evidence for mixing at the interface consistent with growth/recrystallization processes. Isotopic image analyses were performed on select particles from the loose powder experiments for ^{57}Fe-reacted specimens (i.e., ^{57}Fe-hematite and ^{57}Fe-oxalate-hematite) and the control sample (^{NA}Fe-oxalate-hematite) using a Cameca NanoSIMS 50L. The particles were dispersed on vitreous carbon planchets. Individual particles were imaged using SEM to examine their morphology prior to NanoSIMS characterization to aid in correlating site-specific isotopic compositions.

For NanoSIMS isotopic imaging, a 16 keV, ~4 pA Cs^+ primary ion beam with a diameter of ~150 nm was employed for isotopic imaging to observe compositions across the particle surface. The two-dimensional image dimensions were set to encompass a portion of the particle, typically at 10 – 15 μm at 512 × 512 pixels, to obtain higher resolution maps. The entrance slit, aperture slit, and exit slits were set to 20 μm, 350 μm, and 100 μm respectively. NMR regulation was employed in all analyses. Secondary FeO^- ions were accelerated to 8 keV, and $^{57}Fe^{16}O^-$ and $^{57}Fe^{16}O^-$ were detected simultaneously using two

electron multiplier detectors. The iron isotopic composition was determined as $^{57}Fe^{16}O^{-}/^{54}Fe^{16}O^{-}$, hereafter referred to as just "$^{57}Fe/^{54}Fe$."

For the Fe isotopic measurements, ROIs from the control specimen (i.e., ^{NA}Fe(II)-oxalate-hematite) were used as a standard to calibrate the instrument to NA Fe isotopic ratios. Particular emphasis was paid to resolve $^{57}Fe^{16}O^{-}$ from $^{56}Fe^{16}O^{1}H^{-}$, checking the 73 mass peak frequently for drift and re-centering onto the $^{57}Fe^{16}O$ signal as needed; i.e., at least one measurement was conducted on the control at the beginning of every daily analytical session. Instrumental mass fractionation corrections were implemented using the unreacted hematite particles as an external standard, accounting for any artificial changes in isotopic ratios produced during the measurement. The propagated uncertainty (σ) was also calculated to account for variability based on counting statistics for an individual ROI as well as the instrumental mass fraction (IMF) correction factor. Deviations of the $^{57}Fe/^{54}Fe$ isotopic ratios from NA were also considered. That is, variations in isotopic ratios can potentially result from relative differences in ROI heights and orientations, for instance, which impacts sputtered yields, secondary ion counts, and secondary ion energies.[4] Previous studies using SIMS have shown that there is a potential instrumental bias affecting high precision $\delta^{18}O$ measurements for magnetite[5] and $\delta^{56}Fe$ measurements for hematite[6] due to crystal orientation effects. Crystal orientation likely contributed to our uncertainties; however, these effects are small compared to the response observed in the ^{57}Fe-hematite treatment. As mentioned in the main text, $^{57}Fe/^{54}Fe$ ratios on control particles at various orientations and heights for the standard unreacted particles were found to be within uncertainty of NA (0.36); i.e., the average $^{57}Fe/^{54}Fe$ for both the basal and edge surfaces was 0.36±0.01 (considering 2σ, 95% confidence interval). Furthermore, the isotopic contrast for the ^{57}Fe-reacted particles is significant and outside the uncertainty produced from these effects.

Measurements were collected on 2-3 particles per reaction. In all cases, trends in isotopic compositions were observed to be consistent with one another. One representative particle from each reaction is described in the main text. Fe isotopic image processing was performed using the OpenMIMS plugin for ImageJ.[7] Images were pixel by pixel dead time–corrected.[8] Hue-saturation-intensity maps of

$^{57}Fe/^{54}Fe$ were used to visualize the extent of ^{57}Fe-enrichment across the particles. A median filter with a ten-pixel radius was applied to the HSI images to reduce noise. While this makes the image data easier to interpret, it also causes minor visual artefacts due to spatial dilution of signals, such as mottling in the isotopic maps leading to the appearance of island-like isotopic regions. However, these visual artefacts do not extend to the ROI analyses which quantify counts of $^{57}Fe^{16}O^-$ and $^{54}Fe^{16}O^-$ without smoothing. Further, analysis of the control nonetheless enables interpretation of isotopic enrichment and trends between different ^{57}Fe-reacted specimens.

2.4 APT analysis

To determine whether ^{57}Fe deposition on the (001) surface exists at depth, we used three-dimensional atom probe tomography (3D APT) to probe the distribution of ^{57}Fe, focusing on the pyramidal features for the ^{57}Fe-oxalate-hematite specimen. APT measurements and analyses are guided by previous measurements for ^{57}Fe-(001) hematite interface,[9] to which the reader is referred for further discussion on the development of the analysis approach. In brief, for the APT tip preparation, the particles were dispersed onto Si wafers and coated with Cr and Ni (50 – 100 nm of each), using an ion beam sputter deposition system, to protect the particle surface during tip milling. Conventional FIB milling and lift-out techniques for APT specimen preparation using a dual-beam focused-ion beam (FIB) SEM microscope (FEI Helios Nanolab600i). Following Cr-Ni deposition, a particle with well-defined pyramids at the (001) surface was selected for APT analyses using SEM (Figure S2a). The pyramids were marked with Pt deposited as circles, enabling tracing the pyramid during the milling process (Figure S2b). A protective Pt capping layer was deposited on top of the markers to further protect the surface from damage and Ga contamination during ion milling. A lamellar wedge section (~20 μm long) containing the pyramids was created by trench milling on both sides with the ion beam (Ga+ ion, 30 kV), lifted-out, and was extracted with the Omniprobe micromanipulator, and sections with the pyramids were mounted onto Si microposts (Figure S2c, d). The sections with the pyramids were annular milled to obtain needle-

shaped APT specimens with <100 nm tip diameter, monitoring and centering the milling at the Pt markers to capture as close to the pyramid apex as possible (Figure S2e, f). The tips were also intentionally milled such that the topmost layer included Cr to capture the surface of the pyramids.

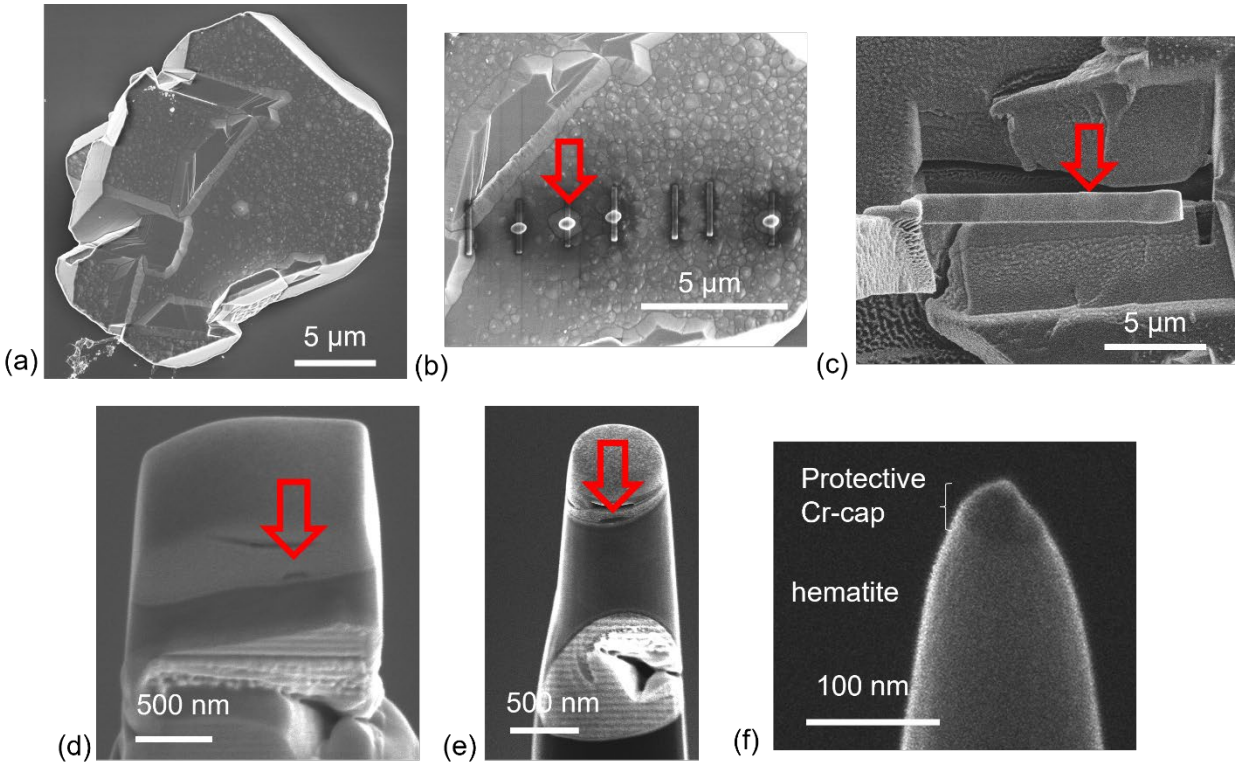

Figure S 2: APT specimen preparation of ^{57}Fe-oxalate-hematite particle by FIB-SEM. (a, b) Particle selected for analyses, where features of interest are marked by Pt shapes (e.g., circles for large pyramids). Red arrow correlates to the pyramidal feature analyzed in the main text. (c) Milling, liftout, and (d) sectioning of the lamella containing features of interest onto Si microposts. (e, f) Annular milling to form the needle-shaped specimen, while monitoring the Pt markers and layers of interest (e.g., protective Cr-coating and hematite).

APT was performed using a CAMECA local electrode atom probe (LEAP) 4000 X-HR at a base temperature and pressure of 40 K and < 2×10^{-11} Torr, respectively. Field evaporation of ions from the specimen was induced by a 355 nm wavelength picosecond laser at a pulse repetition rate of 125 kHz. A detection rate of 0.003–0.005 ions per pulse was maintained by varying the applied specimen voltage.

From previous experience on APT characterization of Fe oxides a laser pulse energy of 40 pJ was selected and provided high data quality and a reasonable sample yield.

Data were reconstructed in 3D by employing the integrated visualization and analysis software (IVAS 3.8.0) developed by CAMECA (Madison, WI). An average atomic volume of 10^{-2} nm^3 $atom^{-1}$ was specified in the 3D reconstruction, representing the atomic density in the hematite lattice (i.e., 99.1 atoms nm^{-3}). The reconstructions were further optimized by fitting it to the tip profile obtained from SEM imaging. A voxel size of 1.0×1.0×1.0 nm and delocalization of 3.0×3.0×1.5 nm was applied.

The 3D chemical and isotopic reconstruction was used to determine the spatial and temporal distribution of ^{57}Fe within a pyramid surface of the ^{57}Fe-oxalate-hematite sample. The protocol for the chemical and isotopic analyses used here has been previously established,[9] which the reader is referred to for detailed descriptions. In brief, ionic Fe and FeO_x species were assigned to their respective mass-to-charge state peaks in the generated mass spectra to obtain the 3D chemical composition. The iron isotopic composition was monitored using the Fe^{++} species, which has consistently been show to satisfactorily reproduce the expected Fe isotopic ratios in NA samples and to not suffer from polyatomic or isobaric interferences.[9, 10] To visualize and quantify local Fe isotopic variations in the reconstructed 3D volume, the mass peaks for ^{56}Fe (28.0 Da) and ^{57}Fe (28.5 Da) within the Fe(II) species subset was assigned a unique isotope identity. The isotopic concentration was analyzed at depth using the proximity histogram method relative to the Cr-hematite interface.[11] The distribution of ^{57}Fe relative to ^{56}Fe is observed through the 3D chemical reconstruction as well as 2D concentration plots of f_{57Fe} (calculated from separate 2D concentration plots for $^{56}Fe^{++}$ and $^{57}Fe^{++}$ generated in IVAS).

Statistical analyses and random comparator techniques were also applied to characterization the distribution of ^{57}Fe, as done in Taylor*, et al.* [9]. In brief, the distribution of ^{57}Fe in the experimental system is compared to a simulated system where the ^{57}Fe distribution is randomized, where spatial correlation in the way the different atomic species occur throughout the data are effectively removed

while maintaining the geometry and bulk composition of the original experiment. The relative strength of randomness is determined by calculating the Pearson coefficient μ (Eqn. 3, 4):

$$\mu = \sqrt{\frac{\chi^2}{N+\chi^2}} \qquad (3)$$

$$\chi^2 = \sum_{n=0}^{n_b} \frac{(e(n)-f(n))^2}{f(n)} \qquad (4)$$

where N is the number of discrete blocks, χ^2 describes the experimental deviation from randomness, $e(n)$ is the number of blocks at concentration n measured experimentally and similarly $f(n)$ is that observed when the atoms are randomly distributed at the surface. Values of μ closer to 0 indicate a random atomic distribution, i.e., like that within the bulk hematite crystal at NA. Values of μ closer to 1 indicate non-random distributions and in turn may suggest phenomena relating to recrystallization-related such as local atomic clustering/segregation upon incorporation.

Supplementary references

1. J. Riemer, H. H. Hoepken, H. Czerwinska, S. R. Robinson and R. Dringen, Colorimetric ferrozine-based assay for the quantitation of iron in cultured cells, *Analyt. Biochem.*, 2004, **331**, 370-375.
2. P. Klapetek, D. Nečas and C. Anderson, Gwyddion, http://gwyddion.net/).
3. S. D. Taylor, L. Kovarik, J. B. Cliff and K. M. Rosso, Facet-selective adsorption of Fe(II) on hematite visualized by nanoscale secondary ion mass spectrometry, *Environ. Sci. Nano*, 2019, DOI: 10.1039/C9EN00562E.
4. F. A. Stevie, *Secondary ion mass spectrometry: Applications for depth profiling and surface characterization*, Momentum Press LLC, New York, NY, 2016.
5. J. M. Huberty, N. T. Kita, R. Kozdon, P. R. Heck, J. H. Fournelle, M. J. Spicuzza, H. F. Xu and J. W. Valley, Crystal orientation effects in $\delta^{18}O$ for magnetite and hematite by SIMS, *Chem. Geol.*, 2010, **276**, 269-283.
6. N. T. Kita, J. M. Huberty, R. Kozdon, B. L. Beard and J. W. Valley, High-precision SIMS oxygen, sulfur and iron stable isotope analyses of geological materials: Accuracy, surface topography and crystal orientation, *Surf Interface Anal*, 2011, **43**, 427-431.
7. M. D. Abràmoff, P. Magelhaes and S. Ram, Image processing with ImageJ, *Biophotonics International*, 2004, **11**, 36-42.
8. OpenMIMS, https://github.com/BWHCNI/OpenMIMS/wiki).
9. S. D. Taylor, J. Liu, B. W. Arey, D. K. Schreiber, D. E. Perea and K. M. Rosso, Resolving iron(II) sorption and oxidative growth on hematite (001) using atom probe tomography, *J. Phys. Chem. C*, 2018, **122**, 3903-3914.

10. S. D. Taylor, J. Liu, X. Zhang, B. W. Arey, L. Kovarik, D. K. Schreiber, D. E. Perea and K. M. Rosso, Visualizing the iron atom exchange front in the Fe(II)-catalyzed recrystallization of goethite by atom probe tomography, *P. Natl. Acad. Sci.*, 2019, **116**, 2866.
11. O. C. Hellman, J. A. Vandenbroucke, J. Rusing, D. Isheim and D. N. Seidman, Analysis of three-dimensional atom-probe data by the proximity histogram, *Microsc. Microanal.*, 2000, **6**, 437-444.